PERGAMON

International Journal of Multiphase Flow 28 (2002) 1497–1519

International Journal of Multiphase Flow

www.elsevier.com/locate/ijmulflow

Terminal velocity of single bubbles in surface tension force dominant regime

A. Tomiyama [a,*], G.P. Celata [b], S. Hosokawa [a], S. Yoshida [a]

[a] *Graduate School of Science and Technology, Kobe University, Rokkodai, Nada, Kobe 657-8501, Japan*
[b] *ENEA, Institute of Thermal-Fluid Dynamics, Via Anguillarese, 301, Rome, Italy*

Received 14 September 2001; received in revised form 5 February 2002

Abstract

Terminal velocity V_T of a single bubble rising through an infinite stagnant liquid in surface tension force dominant regime was investigated theoretically and experimentally. A theoretical V_T model, which is applicable to a distorted spheroidal bubble with a high bubble Reynolds number, was deduced from a jump condition and a potential flow theory for a flow about an oblate spheroid. Experiments were conducted using air and water to measure bubble trajectories, shapes and velocities. As a result, it was confirmed that (1) the primal cause of widely scattered V_T in this regime is not surfactant concentration but initial shape deformation, (2) small initial shape deformation results in a low V_T and a high aspect ratio, whereas large initial shape deformation results in a high V_T and a low aspect ratio, (3) the primal role of surfactants in this regime is to cause the damping of shape oscillation, by which a contaminated bubble behaves as if it were a clean bubble with low initial shape deformation, and (4) the proposed model gives good predictions of V_T for single distorted bubbles.

Keywords: Terminal velocity; Single bubble; Initial shape deformation; Aspect ratio; Surfactants

1. Introduction

Terminal velocity V_T of a single bubble rising through an infinite stagnant liquid is of fundamental importance in the field of gas–liquid two-phase flows. A number of studies (e.g., Clift et al., 1978; Magnaudet and Eames, 2000) therefore have been conducted to establish a reliable V_T model. As for the theoretical models, reliable V_T models are available for two extreme cases, i.e.

* Corresponding author. Tel.: +81-78-803-6131; fax: +81-78-803-6155.
E-mail address: tomiyama@mech.kobe-u.ac.jp (A. Tomiyama).

0301-9322/02/$ - see front matter
PII: S0301-9322(02)00032-0

for small spherical bubbles and large spherical-cap bubbles. When a bubble is small enough to be spherical and the bubble Reynolds number of which is less than unity, V_T can be evaluated by using the Hadamard–Rybczynski solution (Batchelor, 1967). However this solution is valid only for a small spherical bubble in a pure system. If surfactants are accumulated on bubble surface, the so-called Marangoni effect makes the interface immobile, and thereby the bubble behaves as if it were a rigid sphere. In this case, the well-known Stokes drag model can be utilized for the evaluation of V_T. When a bubble is large enough to form a spherical-cap shape, V_T is governed by the inertial force, i.e. by a more or less constant form drag. Davies and Taylor (1950) proposed a theoretical V_T model for spherical-cap bubbles based on a potential flow solution for a flow about a sphere. The use of the potential flow theory is valid at least in the vicinity of the nose of a bubble because the inertial force is much larger than the viscous force and no boundary layer is formed in the vicinity of the bubble nose. Surfactants do not influence V_T, since the form drag is by far superior to the skin friction. Their model therefore agrees well with measured terminal velocities for large single bubbles in pure and contaminated liquids.

In contrast to these two extremes, no theoretical V_T models have been proposed for a bubble of intermediate size, in which the surface tension force plays a dominant role. In the case of an air–water system at atmospheric pressure and room temperature, bubbles ranging from 1.3 to about 6 mm in sphere-volume equivalent diameter d may correspond to a surface tension force dominant regime, in which V_T gradually decreases with increasing d (Peebles and Garber, 1953). Most of bubbles in practical applications therefore fall into this regime. Nonrectilinear motion such as zigzag and helical paths, time-dependent distorted bubble shapes and widely scattered V_T characterize this regime (Aybers and Tapucu, 1969; Zun and Groselj, 1996; Lunde and Perkins, 1998; Magnaudet and Eames, 2000; Ellingsen and Risso, 2001). Although the difference in measured V_T among different experiments has been attributed to the difference in surfactant concentration, there is no firm evidence for this explanation. Aybers and Tapucu (1969) measured rising velocities of single air bubbles in stagnant tap water, and concluded that the effect of surfactants on the rising velocity is very small for bubbles larger than 1.3 mm, whereas bubble shape oscillation has an important effect on the rising velocity. Lunde and Perkins (1998) reported that surfactants cause a dramatic effect on bubbles in the surface tension force dominant regime, that is, contaminated bubbles exhibit only zigzag motions and shape oscillations vanish. However they did not make any statements for the effect of surfactants on V_T. Zhang and Finch (2001) recently examined the effects of surfactant concentration on V_T of 0.8 and 1.4 mm bubbles, and found out that V_T is independent of surfactant concentration. Ellingsen and Risso (2001) carried out an intensive study on 2.5 mm air bubbles in tap water. They pointed out that small initial perturbation applied on bubble surface develops the primary unstable mode which causes a plane zigzag motion, then the secondary unstable mode causing a helical motion grows, and thereby when strong initial perturbation is applied on a bubble, it is possible to observe a helical motion without observing a preceding transitory zigzag motion (Saffman, 1956). Judging from these previous studies, there is a possibility that the scatter of V_T in the surface tension force dominant regime is not caused by the difference in surfactant concentration but by the difference in initial conditions, i.e. the way of bubble release.

In this study, terminal velocity of a single distorted bubble in the surface tension force dominant regime was investigated theoretically and experimentally, while paying attention to bubble shapes and the way of bubble release. To deduce a theoretical V_T model, we assumed a distorted

oblate spheroidal shape and extended the Davies and Taylor's approach by taking a surface tension force into account. Experiments on single air bubbles in distilled water or in water contaminated with surfactants were conducted to verify the proposed model and to examine the effects of initial conditions and surfactants on terminal velocity.

2. Theory

When there is no phase change and the surface tension σ is constant, the momentum jump condition on a gas–liquid interface is given by (Ishii, 1975)

$$P_G \boldsymbol{n} - \tau_G \cdot \boldsymbol{n} = P_L \boldsymbol{n} - \tau_L \cdot \boldsymbol{n} + \sigma\kappa \boldsymbol{n} \tag{1}$$

where the subscripts G and L denote the gas and liquid phases, respectively, P is the pressure, τ the viscous stress tensor, κ the sum of two principal curvatures of the interface, and $\boldsymbol{n}$ the unit normal to the interface which directs from the gas phase to the liquid phase. When a viscous force F_V acting on a bubble is much smaller than forces due to surface tension and inertia, F_S and F_i, the tangential component of Eq. (1) vanishes and the normal component reduces to the well-known Laplace equation:

$$P_G = P_L + \sigma\kappa \tag{2}$$

The assumption of $F_V \ll F_S, F_i$ would be valid at least for a frontal portion of a single bubble rising through a stagnant liquid, provided that the bubble Reynolds number Re satisfies

$$Re \equiv \frac{\rho_L V_T d}{\eta_L} \gg 1 \tag{3}$$

where ρ is the density and η the viscosity.

Then let us apply Eq. (2) to a distorted oblate spheroidal bubble shown in Fig. 1(a). Its major axis is a and the minor axes are b and βb. The parameter β enables us to express various bubble shapes such as a dimpled hemispheroidal-cap ($-1 < \beta < 0$), a hemispheroidal-cap ($\beta = 0$), a distorted spheroid ($0 < \beta < 1$, $\beta > 1$) and a spheroid ($\beta = 1$). A dimpled hemispherical-cap and a hemispherical-cap can be also expressed by setting $a = b$. Then let us define an aspect ratio E by

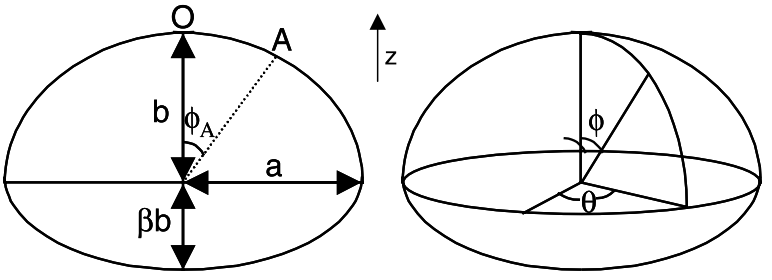

(a) Distorted oblate spheroid (b) Surface coordinates (θ, ϕ)

Fig. 1. Dimensions and coordinates of a distorted bubble ($\beta > -1$): (a) distorted oblate spheroid and (b) surface coordinates (θ, ϕ).

$$E = \frac{b + \beta b}{2a} \tag{4}$$

and an aspect ratio E_f for the frontal part of the bubble by

$$E_f = \frac{b}{a} \tag{5}$$

The two aspect ratios satisfy

$$E_f = \frac{2}{1+\beta} E = \gamma E \tag{6}$$

where γ is a distortion factor defined by

$$\gamma = \frac{2}{1+\beta} \tag{7}$$

The sphere-volume equivalent bubble diameter d satisfies

$$\frac{\pi d^3}{6} = \frac{2\pi}{3}(ba^2 + \beta b a^2) \tag{8}$$

from which we obtain

$$a = \frac{d}{2E^{1/3}} = \frac{d\gamma^{1/3}}{2E_f^{1/3}} \tag{9}$$

and

$$b = \frac{d\gamma E^{2/3}}{2} = \frac{d\gamma^{1/3} E_f^{2/3}}{2} \tag{10}$$

With the surface coordinates ϕ and θ shown in Fig. 1(b), the bubble surface is expressed as

$$\begin{aligned} x &= p(\phi)\cos\theta \\ y &= p(\phi)\sin\theta \\ z &= q(\phi) \end{aligned} \tag{11}$$

where (x, y, z) are Cartesian coordinates and

$$p(\phi) = a\sin\phi \tag{12}$$

$$q(\phi) = b\cos\phi \tag{13}$$

In the frame of reference moving with the bubble, the bubble nose is a stagnant point. Hence by applying the Bernoulli's theorem to the points $O[\phi = 0]$ and $A[\phi = \phi_A (< \pi/2)]$ in Fig. 1(a), we obtain

$$P_{L,O} = P_{L,A} + \tfrac{1}{2}\rho_L u_{L,A}^2 - \tfrac{1}{2}\rho_L g d\gamma^{1/3} E_f^{2/3}(1 - \cos\phi_A) \tag{14}$$

where $u_{L,A}$ is the tangential component of liquid velocity at point A and g the acceleration of gravity. On the other hand, the pressure inside the bubble satisfies

$$P_{G,O} = P_{G,A} - \tfrac{1}{2}\rho_G g d \gamma^{1/3} E_f^{2/3}(1 - \cos\phi_A) \tag{15}$$

Subtracting Eq. (14) from Eq. (15) and substituting Eq. (2) into the resultant equation yield

$$\tfrac{1}{2}\rho_L u_{L,A}^2 = \sigma(\kappa_A - \kappa_O) + \tfrac{1}{2}\Delta\rho g d \gamma^{1/3} E_f^{2/3}(1 - \cos\phi_A) \tag{16}$$

where

$$\Delta\rho = \rho_L - \rho_G \tag{17}$$

The curvatures κ_O and κ_A at points O and A can be evaluated using the following formula of differential geometry:

$$\kappa = -\frac{p'q'' - p''q'}{(p'^2 + q'^2)^{3/2}} - \frac{q'}{p(p'^2 + q'^2)^{1/2}} \tag{18}$$

where the prime denotes the differentiation with respect to ϕ. Substituting Eqs. (9), (10), (12), (13) into Eq. (18) yields

$$\kappa = \frac{2E_f^{4/3}}{d\gamma^{1/3}}\left[\frac{1}{f(m, E_f)} + \frac{1}{f(m, E_f)^3}\right] \tag{19}$$

where

$$m = \cos\phi \tag{20}$$

and

$$f(m, E_f) = \sqrt{m^2 + E_f^2(1 - m^2)} \tag{21}$$

Hence

$$\sigma(\kappa_A - \kappa_O) = \frac{2\sigma E_f^{4/3}}{d\gamma^{1/3}}\left[\frac{1}{f(m_A, E_f)} + \frac{1}{f(m_A, E_f)^3} - 2\right] \tag{22}$$

where

$$m_A = \cos\phi_A \tag{23}$$

To evaluate $u_{L,A}$ in Eq. (16), let us make use of a velocity potential Φ for an axisymmetric potential flow about a bubble moving with the velocity (0, 0, V_T) in the z direction. As noted before, the use of the potential flow theory is valid in the vicinity of the bubble nose under the assumption of $Re \gg 1$. The analytical solution for a potential flow about a moving oblate spheroid with the aspect ratio E_f is readily deduced by making use of the following orthogonal coordinate system (ζ, m, θ):

$$\begin{aligned} x &= k\cosh\chi\sin\phi\cos\theta = k\sqrt{1-\zeta^2}\sqrt{1-m^2}\cos\theta \\ y &= k\cosh\chi\sin\phi\sin\theta = k\sqrt{1-\zeta^2}\sqrt{1-m^2}\sin\theta \\ z &= k\sinh\chi\cos\phi = k\zeta m \end{aligned} \tag{24}$$

where k is a constant and

$$\zeta = \sinh \chi \tag{25}$$

Note that $\zeta = \text{const.}$ constitutes a surface of spheroid with an aspect ratio $\zeta/\sqrt{1-\zeta^2}$ and a constant m corresponds to a hyperboloid. In this coordinate system, the velocity components u_ζ and u_m in ζ (normal) and m (tangential) directions are given by

$$u_\zeta = \frac{1}{k}\sqrt{\frac{\zeta^2+1}{\zeta^2+m^2}}\frac{\partial \Phi}{\partial \zeta} \tag{26}$$

$$u_m = -\frac{1}{k}\sqrt{\frac{1-m^2}{\zeta^2+m^2}}\frac{\partial \Phi}{\partial m} \tag{27}$$

According to Lamb (1932), the velocity potential Φ for an inviscid incompressible flow about a moving spheroid with the minor axis $b = k\zeta_0$ and the major axis $a = k(1-\zeta_0^2)^{1/2}$ is given by

$$\Phi = Qm(1 - \zeta \cot^{-1}\zeta) \tag{28}$$

where

$$Q = \frac{kV_\mathrm{T}}{\zeta_0(\zeta_0^2+1)^{-1} - \cot^{-1}\zeta_0} \tag{29}$$

Substituting Eqs. (28) and (29) into Eqs. (26) and (27) yields the following normal and tangential components of liquid velocity on the surface of spheroid, i.e. at $\zeta = \zeta_0$.

$$u_\zeta = V_\mathrm{T} m\sqrt{\frac{\zeta_0^2+1}{\zeta_0^2+m^2}} \tag{30}$$

$$u_m = V_\mathrm{T}\sqrt{\frac{1-m^2}{\zeta_0^2+m^2}}\frac{1-\zeta_0\cot^{-1}\zeta_0}{\zeta_0(\zeta_0^2+1)^{-1} - \cot^{-1}\zeta_0} \tag{31}$$

The liquid velocity on the bubble front surface in the frame of reference moving with the spheroidal bubble can be deduced by subtracting $-V_\mathrm{T}\mathbf{e}_z$ from the above equations. Here $\mathbf{e}_z$ is the unit vector in the z direction. The z components of the unit outward normal $\boldsymbol{n}$ and unit tangential $\boldsymbol{t}$ to the surface of spheroid are given by $m((\zeta_0^2+1)/(\zeta_0^2+m^2))^{1/2}$ and $-\zeta_0((1-m^2)/(\zeta_0^2+m^2))^{1/2}$. Hence $-V_\mathrm{T}\mathbf{e}_z$ can be decomposed into the ζ and m components as follows:

$$V_\zeta = -V_\mathrm{T}\mathbf{e}_z \cdot \boldsymbol{n} = -V_\mathrm{T} m\sqrt{\frac{\zeta_0^2+1}{\zeta_0^2+m^2}} \tag{32}$$

$$V_m = -V_\mathrm{T}\mathbf{e}_z \cdot \boldsymbol{t} = V_\mathrm{T}\zeta_0\sqrt{\frac{1-m^2}{\zeta_0^2+m^2}} \tag{33}$$

Consequently, in the frame of reference moving with the distorted bubble, the normal and tangential components, u_n and u_t, of liquid velocity on the frontal part of bubble surface are given by

$$u_n = u_\zeta - V_\zeta = 0 \tag{34}$$

$$u_t = u_m - V_m = V_T \sqrt{\frac{1-m^2}{\zeta_0^2+m^2}} \left[\frac{1}{(\zeta_0^2+1)\cot^{-1}\zeta_0 - \zeta_0} \right] \tag{35}$$

Since $E_f = \zeta_0/\sqrt{1-\zeta_0^2}$, ζ_0 in the above equation can be replaced with $E_f/\sqrt{1-E_f^2}$. As a result, we obtain the following expression for $u_{L,A}$ in Eq. (16):

$$u_{L,A} = V_T \sqrt{\frac{(1-E_f^2)(1-m_A^2)}{f(m_A,E_f)^2}} \left[\frac{1-E_f^2}{\sin^{-1}\sqrt{1-E_f^2} - E_f\sqrt{1-E_f^2}} \right] \tag{36}$$

Substituting Eqs. (22) and (36) into Eq. (16), solving the resultant equation for V_T, and taking the limit $m_A \to 1 (\phi_A \to 0)$ yield

$$V_T = F(E_f) \sqrt{\frac{8\sigma}{\rho_L d}\frac{E_f^{4/3}}{\gamma^{1/3}} + \frac{\Delta\rho g d}{2\rho_L}\frac{\gamma^{1/3}E_f^{2/3}}{1-E_f^2}} \tag{37}$$

where

$$F(\Omega) = \frac{\sin^{-1}\sqrt{1-\Omega^2} - \Omega\sqrt{1-\Omega^2}}{1-\Omega^2} \tag{38}$$

or in terms of E,

$$V_T = F(\gamma E) \sqrt{\frac{8\sigma}{\rho_L d}\gamma E^{4/3} + \frac{\Delta\rho g d}{2\rho_L}\frac{\gamma E^{2/3}}{1-\gamma^2E^2}} \tag{39}$$

The reason for taking the limit is that the assumption of the potential flow is valid at least in the vicinity of the bubble nose. A V_T model including the angle ϕ_A is given in Appendix A.

As is well known, the upper bound of V_T in the surface tension force dominant regime, which may be observed in a pure system, is well correlated with (Mendelson, 1967; Marrucci et al., 1970; Tomiyama et al., 1998)

$$V_T = \sqrt{\frac{2\sigma}{\rho_L d} + \frac{\Delta\rho g d}{2}} \tag{40}$$

The proposed V_T model, Eq. (37) or Eq. (39), takes the similar form with Eq. (40). In addition, it implies that V_T depends not only on d and fluid properties but also on bubble shape, (E,γ) or (E_f,γ), so that if the bubble shape is not uniquely determined by d and fluid properties, V_T would be varied with the shape. In other words, there is a possibility that the cause of the large scatter of V_T in the surface tension force dominant regime lies in bubble shapes.

By substituting Eq. (39) into the force balance

$$C_D \frac{1}{2}\rho_L V_T^2 \frac{\pi d^2}{4} = \Delta\rho g \frac{\pi d^3}{6} \tag{41}$$

we obtain the following drag coefficient C_D:

$$C_D(Eo,\gamma,E) = \frac{2Eo}{\gamma E^{3/2}(1-\gamma^2E^2)Eo + 16\gamma E^{4/3}} F(\gamma E)^{-2} \tag{42}$$

where Eo is the Eötvös number defined by

$$Eo = \frac{\Delta\rho g d^2}{\sigma} \tag{43}$$

Since the proposed V_T model is based on the local instantaneous momentum jump condition and the solution of the Laplace equation $\nabla\Phi = 0$, Eq. (42) would be applicable to an unsteady bubble motion.

3. Experiment

Fig. 2 is a schematic of the experimental setup. The height, width and depth of the tank were 1.0, 0.2 and 0.2 m, respectively. Distilled water or distilled water with a 0.00075% volume fraction of liquid soap was stored in the tank to examine the effect of surfactants on bubble shape, motion and velocity. A measured amount of air was stored in the bubble injection line. A single bubble was released from a nozzle by making use of the static pressure difference between the height of water in the tank and that in the small water container connected to the bubble injection line. The water stored in the small container was the same water with the water in the tank. Four different nozzles were used to produce various bubbles, the inside diameters of which were 0.51, 0.90, 1.45 and 3.19 mm. The static pressure difference was controlled by the elevation of the small container. This bubble release method based on the static pressure difference and several nozzles enabled us to examine the effect of initial shape deformation on bubble characteristics. Large initial shape

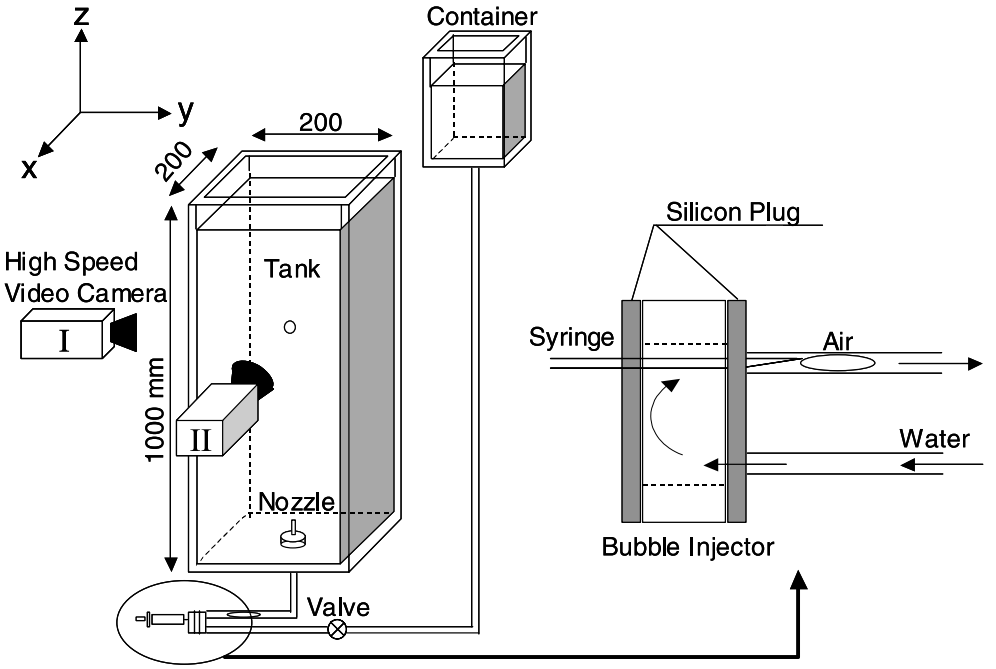

Fig. 2. Experimental setup and bubble injection device.

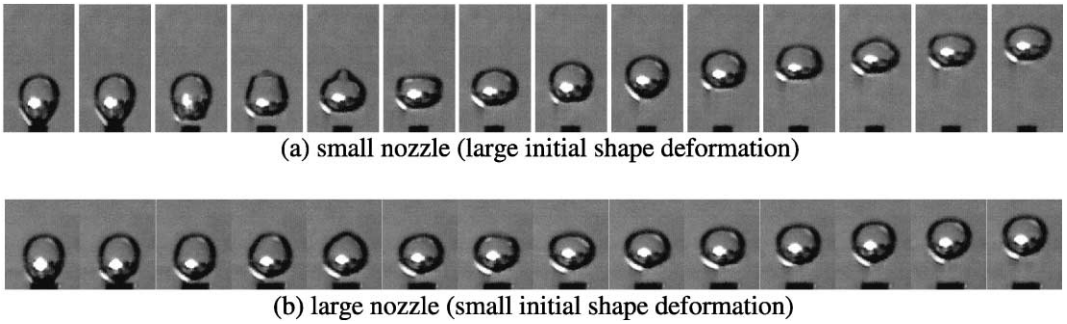

Fig. 3. Detachment of a 3.0 mm bubble (time step between two consecutive images is 0.002 s): (a) small nozzle (large initial shape deformation) and (b) large nozzle (small initial shape deformation).

deformation was realized by releasing a bubble either with a high static pressure difference or with a nozzle, the inside diameter of which is much smaller than d. As an example, single 3.0 mm bubbles released from small and large nozzles are shown in Fig. 3. The bubble detached from the small nozzle (Fig. 3(a)) was more deformed than the bubble from the large nozzle (Fig. 3(b)).

Two high-speed digital video cameras (Kodak Motion Corder Analyzer SR-1000, shutter speed = 1/5000 s, frame rate = 250 frames/s, 512×512 pixels in one frame) were used to obtain three-dimensional bubble trajectories, instantaneous bubble velocities, instantaneous aspect ratios, terminal velocities and time-averaged aspect ratios. The camera position and zoom ratio were determined so as to capture more than one wavelength of a fluctuating bubble path within the frame of the camera. Two examples of original bubble images are shown in Fig. 4(a). To improve the quality of the original image, a background image, which was recorded with the absence of a bubble, was subtracted from the original image as shown in Fig. 4(b). Then the improved image was transformed into a binary image (Fig. 4(c)), by which an instantaneous three-dimensional position $\boldsymbol{R}(t) = (x(t), y(t), z(t))$ of the center of bubble area, and total lengths of instantaneous major and minor axes, $A(t) = 2a(t)$ and $B(t) = (1 + \beta)b(t)$, were determined as shown in Fig. 4(d). The measurement error of $\boldsymbol{R}(t)$ depends on the spatial resolution of the original image. One pixel size corresponded to 0.029 mm for bubbles less than 1 mm in d, 0.059 mm for $1 \leqslant d < 1.5$ mm, and 0.098 mm for $d \geqslant 1.5$ mm. As was pointed out by Lunde and Perkins (1998), how to quantify the position and shape of a deformed bubble from its two-dimensional projections is not obvious. It is, in a strict sense, impossible to accurately measure a position of the center of bubble volume,

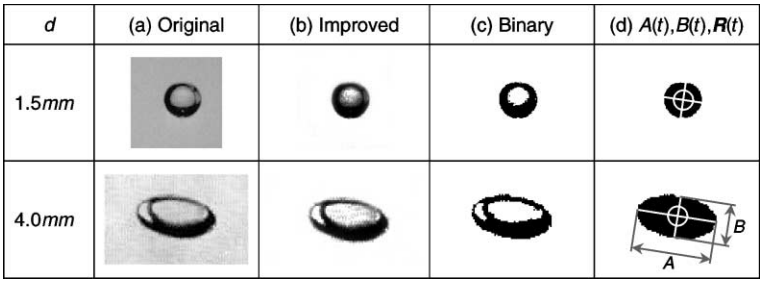

Fig. 4. Determination of bubble position and total lengths of axes, A and B.

$A(t)$ and $B(t)$ from the two-dimensional projections. The camera I in Fig. 2 provided images for evaluating $x(t)$, $z_{\mathrm{I}}(t)$, $A_{\mathrm{I}}(t)$ and $B_{\mathrm{I}}(t)$, whereas the camera II offered images for the evaluation of $y(t)$, $z_{\mathrm{II}}(t)$, $A_{\mathrm{II}}(t)$ and $B_{\mathrm{II}}(t)$. Here the subscripts I and II denote the camera I and II, respectively. The equalities, $z_{\mathrm{I}}(t) = z_{\mathrm{II}}(t)$, $A_{\mathrm{I}}(t) = A_{\mathrm{II}}(t)$ and $B_{\mathrm{I}}(t) = B_{\mathrm{II}}(t)$ would hold if and only if a bubble possesses the axisymmetry. As an example, measured $z_{\mathrm{I}}(t)$, $z_{\mathrm{II}}(t)$, $x(t)$, $y(t)$, $A_{\mathrm{I}}(t)$, $A_{\mathrm{II}}(t)$, $B_{\mathrm{I}}(t)$ and $B_{\mathrm{II}}(t)$ for a 3.0 mm bubble with zigzag motion and a 3.0 mm bubble with helical motion are shown in Fig. 5(a) and (b), respectively. Instantaneous aspect ratios, $E_{\mathrm{I}}(t)$ and $E_{\mathrm{II}}(t)$, and instantaneous velocities, $V_x(t)$, $V_y(t)$, $V_{z\mathrm{I}}(t)$ and $V_{z\mathrm{II}}(t)$, are also shown in the figure. The latter quantities were calculated by using

$$E_{\mathrm{I}}(t) = B_{\mathrm{I}}(t)/A_{\mathrm{I}}(t), \quad E_{\mathrm{II}}(t) = B_{\mathrm{II}}(t)/A_{\mathrm{II}}(t) \tag{44}$$

$$V_x(t) = \frac{x(t+\Delta t) - x(t)}{\Delta t} \tag{45}$$

$$V_y(t) = \frac{y(t+\Delta t) - y(t)}{\Delta t} \tag{46}$$

$$V_{z\mathrm{I}}(t) = \frac{z_{\mathrm{I}}(t+\Delta t) - z_{\mathrm{I}}(t)}{\Delta t}, \quad V_{z\mathrm{II}}(t) = \frac{z_{\mathrm{II}}(t+\Delta t) - z_{\mathrm{II}}(t)}{\Delta t} \tag{47}$$

where $\Delta t = 0.004$ s. As can be understood from this figure, the difference between $z_{\mathrm{I}}(t)$ and $z_{\mathrm{II}}(t)$ was not so large as to cause a significant difference in $V_z(t)$. On the other hand, the difference in the major and minor axes measured by the two cameras caused the maximum difference of about 20% in the instantaneous aspect ratios, $E_{\mathrm{I}}(t)$ and $E_{\mathrm{II}}(t)$. However there was no need to accurately measure instantaneous bubble shapes because the main purpose of this study is not the shape oscillation but the terminal velocity. Hence the evaluation of $E(t)$ was carried out by using images taken with the camera I, and $z(t)$ was evaluated as $z(t) = (z_{\mathrm{I}}(t) + z_{\mathrm{II}}(t))/2$. Uncertainties in $[\boldsymbol{V}_B(t) = (V_x(t), V_y(t), V_z(t)), E(t)]$ estimated based on the spatial resolution of images were [0.007 m/s, 5.2%] for $d < 1$ mm, [0.015 m/s, 4.0%] for $1 \leqslant d < 1.5$ mm, and [0.024 m/s, 8.6%] for $d > 1.5$ mm.

In a wavelength λ of a more or less periodic bubble path, $V_z(t)$ and $E(t)$ exhibit two cycles of fluctuation. Hence the terminal velocity V_{T} was evaluated as the ratio of the distance λ to the time duration T required for a bubble to travel λ, by which uncertainty in measured V_{T} was decreased to ± 0.00137 m/s. A time-averaged aspect ratio E, which will be used in Section 4, was defined as an arithmetic average of $E(t)$ data within λ. Note that the difference between E_{I} and E_{II} i.e. between the mean aspect ratios deduced from images obtained by the camera I and II, was not so large. For example, $(E_{\mathrm{I}}, E_{\mathrm{II}}) = (0.819, 0.823)$ for the data in Fig. 5(a) and (0.739, 0.749) for the data in Fig. 5(b). Hence measured time-averaged aspect ratios might involve less errors than $E(t)$.

Measurements of V_{T} and E were carried out at the elevation about 170 mm above the nozzle tip ($150 < z < 200$ mm). Hereafter the distance from the nozzle tip is denoted by z. To examine whether or not bubbles reach terminal conditions at $z = 170$ mm, terminal velocities were also measured at $z = 900$ mm. Fig. 6 shows comparisons between V_{T} at $z = 170$ mm and V_{T} at $z = 900$ mm for (a) single bubbles in the distilled water and (b) those in the water with surfactants. In both cases, V_{T} at $z = 900$ mm was slightly larger than that at $z = 170$ mm. This slight increase was due to the volume expansion caused by the decrease of static pressure. Hence we could confirm that all the bubbles in the experiments reached the terminal conditions at $z = 170$ mm. According to

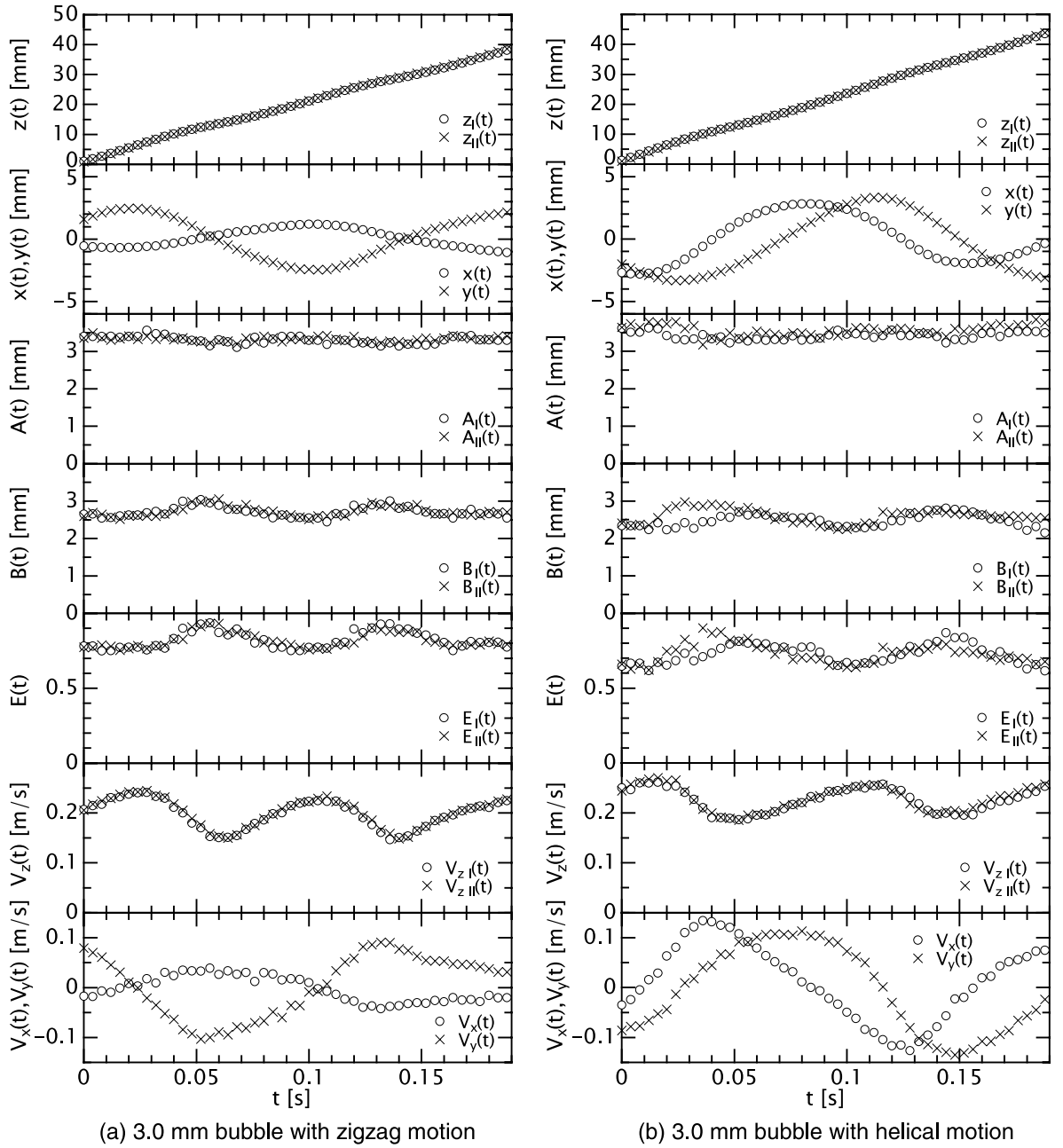

Fig. 5. Instantaneous bubble positions, shapes and velocities deduced from images taken by two cameras: (a) 3.0 mm bubble with zigzag motion and (b) 3.0 mm bubble with helical motion.

Zhang and Finch (2001), the traveling distance to reach a terminal condition depends on surfactant concentration, and it decreases with increasing the concentration. The fact that contaminated bubbles in this study reached the terminal conditions within a short distance ($z < 170$ mm)

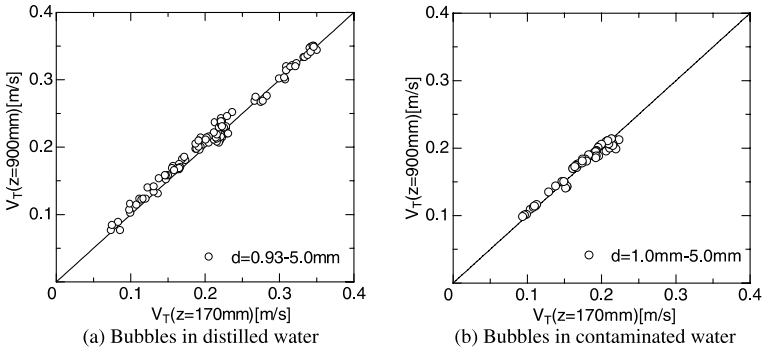

Fig. 6. Comparisons of V_T at two elevations.

therefore implies that the water with a 0.00075% volume fraction of liquid soap was fully contaminated with surfactants.

4. Results and discussion

4.1. Single bubbles in distilled water

As a result of experiments using the distilled water, we confirmed that bubble motion, shape and velocity are markedly sensitive to an initial condition, i.e. the way of bubble release. Except for the remark made by Zhang and Finch (2001), the well-known large scatter of V_T in the surface tension force dominant regime has been attributed to the difference in the amount of surfactants accumulated on bubble surface. However this scatter is not caused by the difference in surfactant concentration but by the difference in initial shape deformation, as will be disclosed in the following.

Fig. 7(a) and (b) are two examples of consecutive bubble images, instantaneous aspect ratios $E(t)$, instantaneous rising velocities V_z, bird's eye and top views of trajectories for 3.0 mm bubbles in distilled water. The time interval of two consecutive images is 0.02 s. As shown in Fig. 7(a), when a bubble was released from a nozzle with small initial shape deformation, the rising velocity V_z was low, the motion was apt to be zigzag, and the aspect ratio kept a high value. To the contrary, when it was released with large initial shape deformation, V_z took a higher value, the motion was likely to be helical, and the aspect ratio kept a low value as shown in Fig. 7(b). As a result, even in the distilled water, measured V_T widely scattered in the surface tension force dominant regime as shown in Fig. 8. It should be noted that terminal velocities for single bubbles with small initial shape deformations are not so much scattered, whereas those for bubbles with large initial shape deformations scatter widely. The multiple terminal conditions might result from a certain kind of bifurcation caused by the nonlinearity in the Navier–Stokes equation and a nonlinear link between the momentum jump condition and Navier–Stokes equation, i.e. the link between the bubble interface and the flow field induced by a bubble itself. The trigger causing the bifurcation might relate with the surface free energy σS, where S is the area of bubble surface. When initial shape deformation is large, bubble shape is stretched as shown in Fig. 3(a). As a

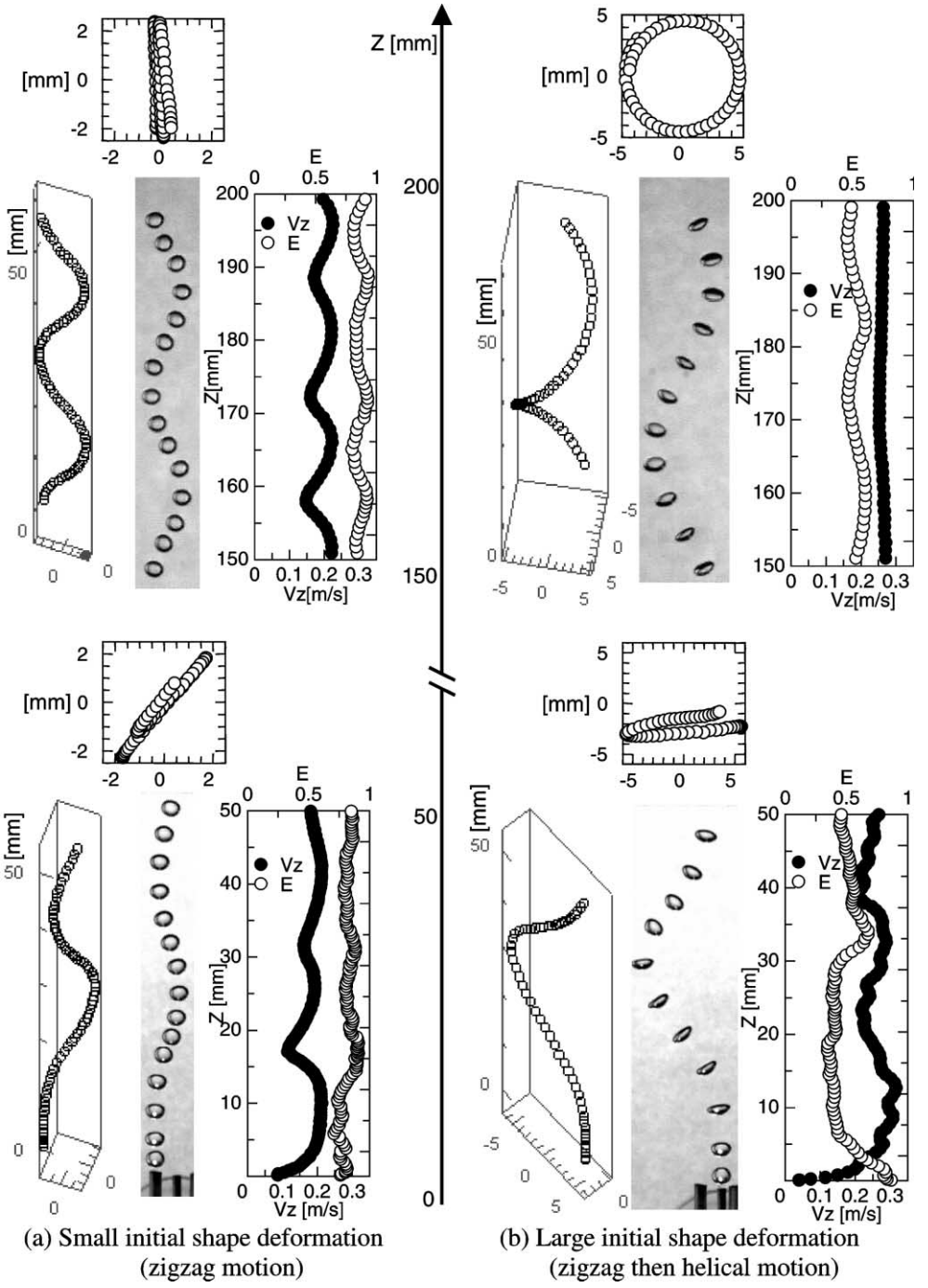

Fig. 7. Consecutive images, top and bird's eye views of trajectory, instantaneous aspect ratio and instantaneous rising velocity of a single air bubble ($d = 3.0$ mm) in distilled water: (a) small initial shape deformation (zigzag motion) and (b) large initial shape deformation (zigzag then helical motion).

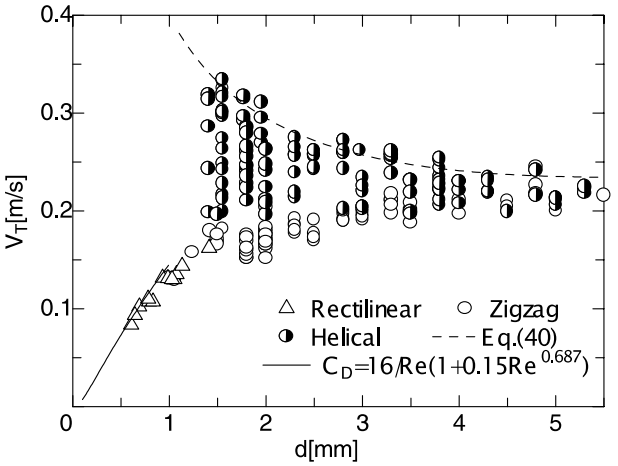

Fig. 8. Measured terminal velocities of single air bubbles in a distilled water. Note that measured V_T for $d < 1.3$ mm agrees with a C_D correlation for a pure system (Tomiyama et al., 1998) and Eq. (40) runs through the upper bound of measured V_T. Motion types were measured at about 170 mm above the nozzle tip.

result, the bubble starts its motion with a surface free energy larger than that of a bubble with small initial shape deformation. Since this is merely a speculation, further study on the cause and trigger of bifurcation must be carried out in the future.

The types of motion in Fig. 8 were determined at the region of $150 \leqslant z \leqslant 200$ mm. Motion types were also observed for several bubbles at $900 \leqslant z \leqslant 950$ mm to examine the occurrence of transition from zigzag to helical motion or vice versa. Results are summarized in Table 1. As has been pointed out by many researchers (e.g., Ellingsen and Risso, 2001; Saffman, 1956; Lunde and Perkins, 1997), only the transition from zigzag to helical motion was observed. Note that even when a bubble with large initial shape deformation exhibited a helical motion at $z \sim 170$ mm, its initial fluctuating motion was apt to be zigzag as shown in Fig. 7(b). These results therefore support the conclusion of Ellingsen and Risso; the primary unstable mode causing zigzag motion develops first and the secondary unstable mode causing helical motion then grows. In other words, large initial shape deformation augments the growth rate of the secondary unstable mode, whereas small initial shape deformation delays the transition from the primary to secondary unstable mode. Hence it would be impossible to predict a motion type only with d and fluid

Table 1
Motion types at $z = 170$ and 920 mm

	Bubble diameter d (mm)		
	2.0	3.0	4.0
Total number of sampled bubbles	56	30	20
Zigzag ($z \sim 170$ mm) to zigzag ($z \sim 920$ mm)	37	8	6
Helical ($z \sim 170$ mm) to helical ($z \sim 920$ mm)	14	21	13
Zigzag ($z \sim 170$ mm) then helical ($z \sim 920$ mm)	5	1	1
Helical ($z \sim 170$ mm) then zigzag ($z \sim 920$ mm)	0	0c	0

properties. As can be understood from Fig. 8 and Table 1, the bubble motion at a certain elevation from a nozzle could be either zigzag or helical, depending on the way of bubble release. Therefore the motion regime suggested by Aybers and Tapucu (1969), i.e. helical in $1.3 < d < 2.0$, zigzag then helical in $2.0 < d < 3.6$, and zigzag in $3.6 < d < 4.2$ mm, must be regarded as merely the outcome of their bubble release method.

Since it was experimentally and theoretically confirmed that V_T depends not only on d but also on the aspect ratio E, the proposed V_T model was compared with the measured V_T. As mentioned in Section 3, the measurement of the distortion factor γ for distorted wobbling bubbles was almost impossible. The comparison was therefore carried out by assuming that bubble shapes were spheroidal, i.e., $\gamma = 1$. With this assumption, Eq. (39) reduces to

$$V_T = \frac{\sin^{-1}\sqrt{1-E^2} - E\sqrt{1-E^2}}{1-E^2}\sqrt{\frac{8\sigma}{\rho_L d}E^{4/3} + \frac{\Delta\rho g d}{2\rho_L}\frac{E^{2/3}}{1-E^2}} \tag{48}$$

As shown in Fig. 9, the proposed model gives good predictions for the effects of d and E on V_T, i.e., V_T decreases with increasing the mean aspect ratio, and the effect of E on V_T within the range of $1.5 \leqslant d \leqslant 5.0$ mm becomes less significant as d increases.

Then the instantaneous bubble rising velocity V_z was calculated by substituting the measured instantaneous aspect ratio $E(t)$ into Eq. (48) to examine the applicability of the proposed V_T model to the evaluation of V_z. Fig. 10 shows comparisons between measured and calculated V_z. Although the calculated V_z does not agree so well with the measured V_z, the trend of velocity fluctuation is well reproduced by the model. The error could be reduced by improving the accuracy of $E(t)$ and by taking account of other transient forces such as a virtual mass force and a lift force caused by wake shedding (de Vries et al., 2001).

4.2. Single bubbles in water contaminated with surfactants

Fig. 11 shows measured V_T in the water contaminated with surfactants. Terminal velocities of contaminated bubbles agree well with those of clean bubbles with small initial shape deformations. As suggested by Lunde and Perkins (1998), contaminated bubbles did not exhibit helical motions even when they were released with large initial shape deformations. Therefore it can be concluded that a contaminated bubble behaves as if it were a clean bubble with small initial shape deformation. This coincidence can be explained by the well-known fact that the damping coefficient of surface tension wave or capillary wave becomes much higher when surfactants are accumulated on the gas–liquid interface (Landau and Lifshitz, 1987). Hence, even if a bubble is released with large initial shape deformation, the shape oscillation caused by the initial deformation rapidly damps down in a fully contaminated system, which results in a high aspect ratio and a low terminal velocity. Several examples of consecutive images of single bubbles in the distilled and contaminated waters are shown in Fig. 12. The time interval of two consecutive bubble images is 0.02 s. The 3.0 mm bubble in the contaminated system was released with large initial shape deformation. However soon after the detachment from the nozzle, its motion became closely similar to the motion of a 3.0 mm clean bubble with small initial shape deformation. In the cases of $d = 4.0$ and 5.0 mm, contaminated bubbles did not exhibit large shape oscillation due to the strong damping effect caused by surfactants. If water is less contaminated with surfactants

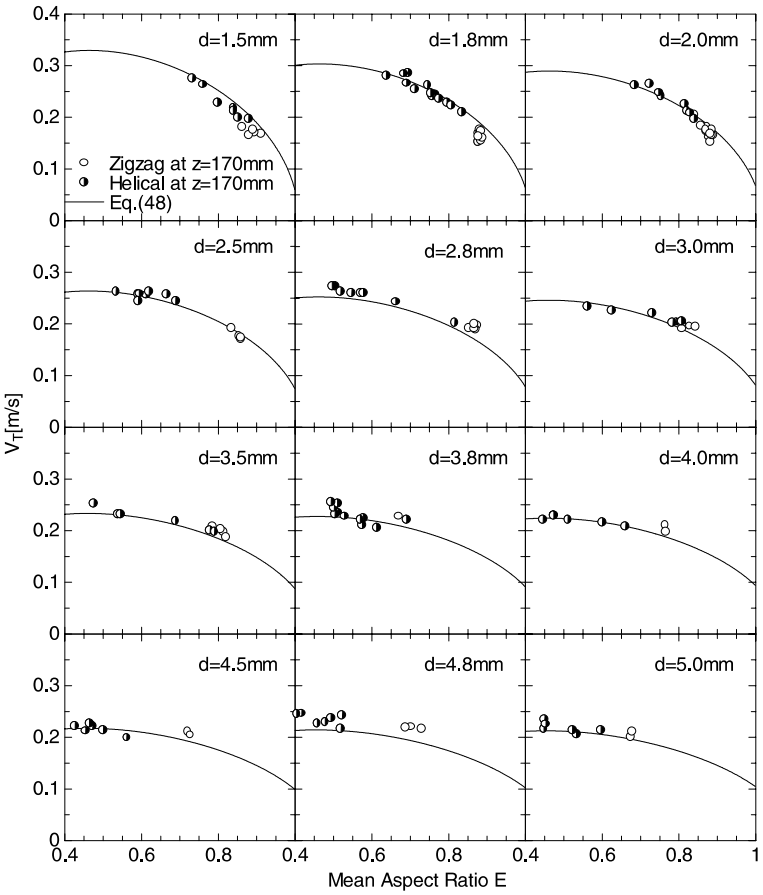

Fig. 9. Comparisons between measured and calculated terminal velocities in distilled water.

than the contaminated water in the present experiment, the damping might not be so rapid. However, judging from the experimental evidence that V_T does not depend on surfactant concentration (Zhang and Finch, 2001), shape oscillation caused by large initial deformation would gradually damp down even in a slightly contaminated system, and when a bubble reaches the terminal condition, it would behave as if it were a clean bubble with low initial deformation.

According to Wellek et al. (1966), the mean aspect ratio E in a fully contaminated system is well correlated by

$$E = \frac{1}{1 + 0.163Eo^{0.757}} \tag{49}$$

The validity of this correlation can be confirmed by Fig. 13, in which the measured mean aspect ratios of contaminated bubbles are plotted against the Eötvös number. The solid curve in Fig. 11 was drawn by using Eqs. (48) and (49). The lower bound of V_T in a fully contaminated system is well traced by the proposed model and Wellek correlation.

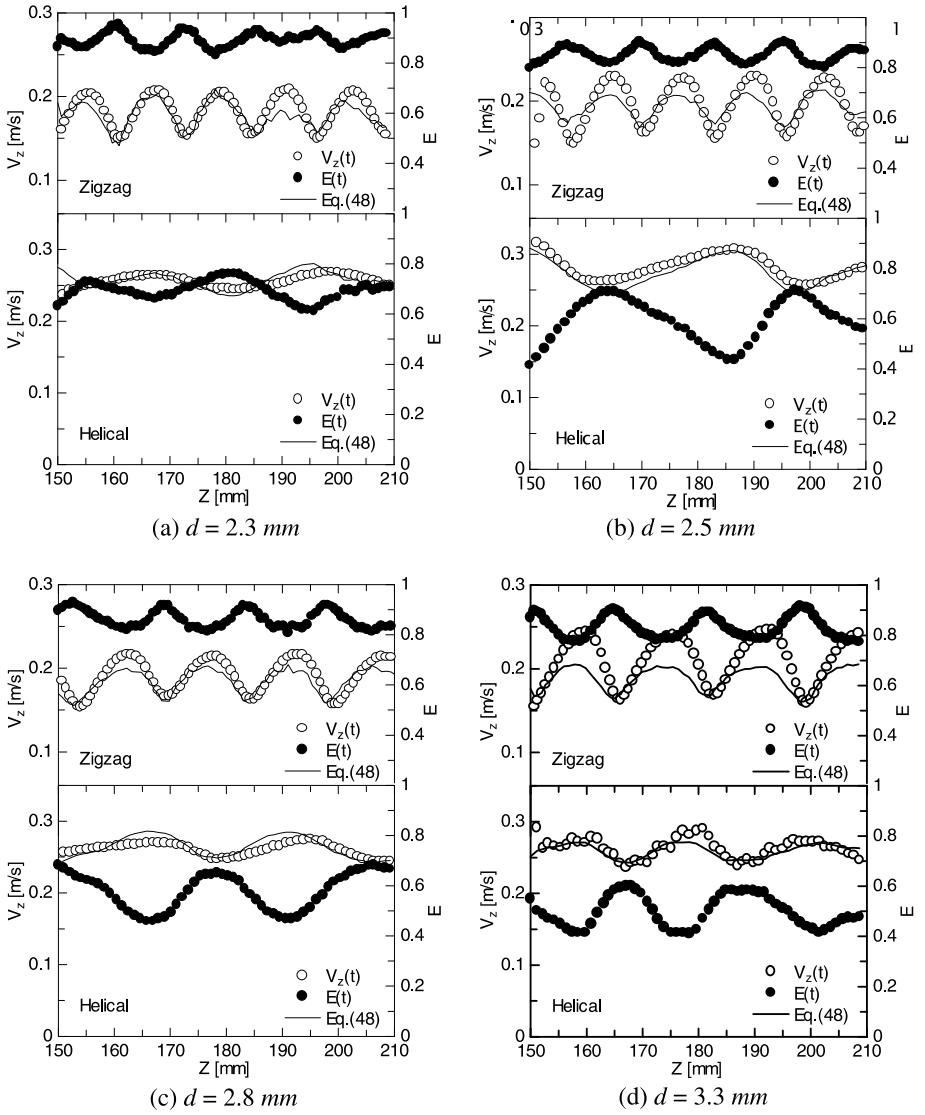

Fig. 10. Application of the proposed model to the evaluation of instantaneous rising velocity.

Now we can summarize the primal role played by surfactants in bubble dynamics as follows:

(I) *Viscous force dominant regime (small spherical bubble):* The accumulation of surfactants on bubble surface induces the so-called Marangoni effect that makes the bubble interface immobile as if it were a rigid sphere. The boundary condition on the interface therefore changes from free-slip to no-slip, which results in the increase in the viscous drag and the decrease in V_T.

(II) *Surface tension force dominant regime (intermediate bubble):* Surfactants damp down the shape oscillation, by which the mean aspect ratio E increases, and thereby V_T becomes close

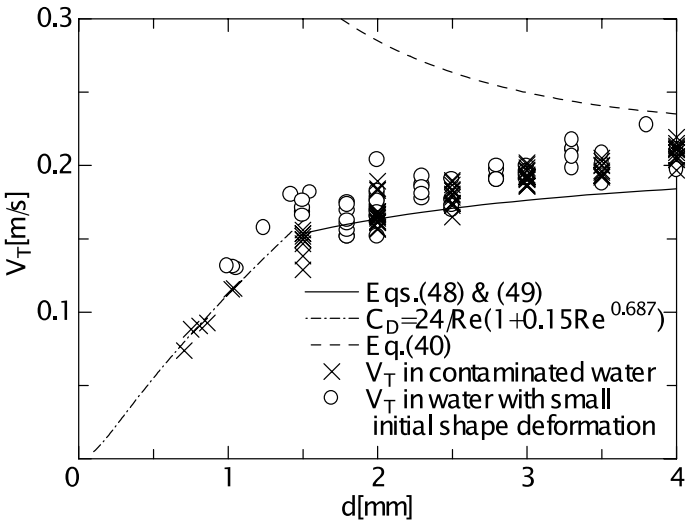

Fig. 11. Measured and calculated V_T in contaminated water, and the measured V_T for bubbles with small initial shape deformation in distilled water quoted from Fig. 8. Note that measured V_T for $d < 1.3$ mm is close to the value calculated by a C_D correlation for a contaminated system (Tomiyama et al., 1998), and high terminal velocities were not obtained even when a bubble was released with large initial shape deformation.

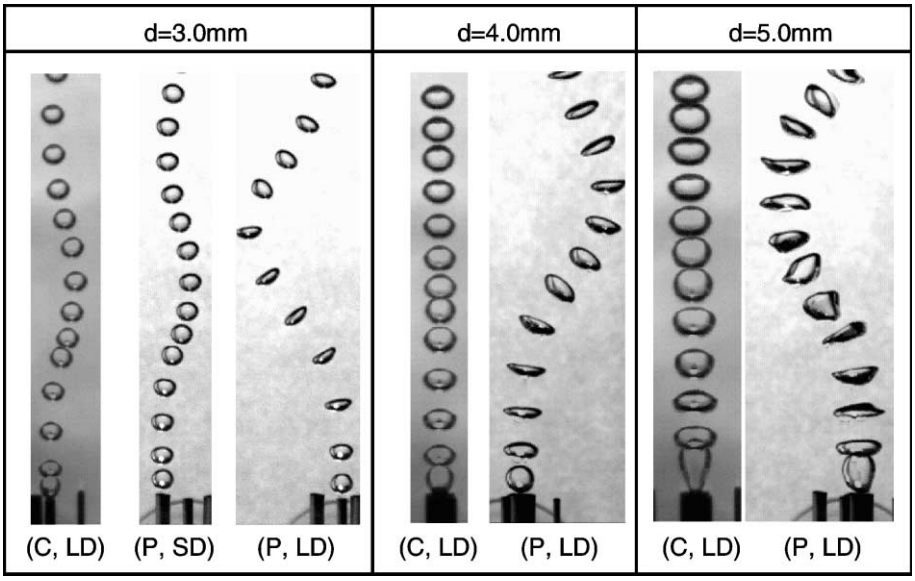

Fig. 12. Shapes and trajectories of single bubbles in pure (P) and contaminated (C) systems: LD—large initial shape deformation; SD—small initial shape deformation.

to that for a clean bubble with small initial shape deformation. Consequently, the scatter of V_T caused by initial shape deformation becomes much smaller than that in a pure system.

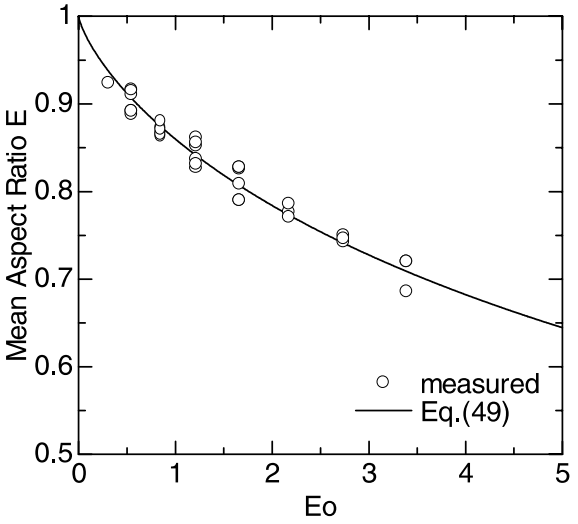

Fig. 13. Comparison between measured mean aspect ratios of fully contaminated bubbles and Eq. (49).

(III) *Inertial force dominant regime (large bubble):* Due to high inertia, the surface tension ceases to play a dominant role in bubble motion and shapes. Although there might be a certain portion of bubble interface where the characteristics of viscous drag F_V is altered by the Marangoni effect, this slight change in F_V has little influence on V_T because the form drag due to inertia is much higher than F_V. Similarly the surface tension force F_S has negligible effects because F_S is proportional to d^{-1} (see Eq. (39)).

Up to the present, the role (II) has not been pointed out, and the role (I) has been postulated even for bubbles in the surface tension force dominant regime. This postulation has caused confusion not only to experimentalists but also to CFD researchers. When we attempt to measure V_T, it is inevitable to release a bubble with a certain magnitude of initial shape deformation. Rather a bubble must be often released with large initial shape deformation. As a result, we may obtain two curves in a d–V_T diagram. The one is constituted by data obtained in a pure system, which is close to Eq. (40). The other is constituted by data obtained in a system contaminated with surfactants, which is close to the lower bound of V_T in Fig. 8. Since we have obtained the two curves and postulated the role (I) even for the surface tension force dominant regime, we are ready to conclude that the immobile interface should be the reason of low V_T in systems contaminated with surfactants. CFD researchers have faced with a trouble in the prediction of V_T. The trouble is that in spite of using "clean" continuity and Navier–Stokes equations, interface tracking simulation is apt to yield V_T close to that of a bubble in a contaminated system. Now this paradox is easy to answer. In interface tracking simulation, a spherical shape is usually assumed as an initial bubble shape. This initial condition corresponds to a bubble with small initial shape deformation so that the predicted V_T is likely to be close to the lower bound of V_T in Fig. 8.

5. Some notes

The closure of the V_T model, Eqs. (37) and (39) or (48) requires a model for evaluating the mean aspect ratio E and the mean distortion factor γ. In this evaluation, we need to solve the continuity and Navier–Stokes equations together with jump conditions under given initial and geometric boundary conditions. Hence it would be very difficult to develop a mathematically closed model of V_T. Therefore a better strategy would be to develop empirical correlations of E and γ for a particular problem of concern. Once the range of E is given as a function of bubble diameter, it is possible to determine the range of terminal velocity by substituting the minimum and maximum values of E into Eq. (48).

One exception might be a mean relative velocity of bubbles in a turbulent bubbly pipe flow. Under the action of bulk liquid turbulence, bubbles would take various aspect ratios. As a result, what one can expect for the mean bubble relative velocity is the mean value of the scattered V_T. As can be understood from Fig. 8, the mean value within $2 < d < 5$ mm is close to 23 cm/s. This value corresponds to the well-known drift velocity given by

$$V_{GJ} = \sqrt{2}\left(\frac{\sigma g \Delta\rho}{\rho_L^2}\right)^{1/4} \tag{50}$$

This might be the reason why the above equation together with a drift-flux correlation (Zuber and Findlay, 1965) yields good predictions of mean void fractions of bubbly upflows. That is to say, even if each bubble in a bubbly flow takes various bubble shapes and relative velocities, we may not have to take them into account for the purpose of evaluating mean relative velocities and mean void fractions in turbulent bubbly flows consisting of bubbles in the surface tension force dominant regime.

6. Conclusions

Terminal velocity V_T of a single bubble rising through an infinite stagnant liquid in a surface tension force dominant regime was investigated theoretically and experimentally. A theoretical V_T model, which is applicable to various kinds of distorted spheroidal bubbles with high bubble Reynolds numbers, was deduced from a momentum jump condition and a potential flow theory for a flow about an oblate spheroid. Experiments were conducted using air and water to measure bubble trajectories, time-dependent shapes and velocities in pure and contaminated systems. The following conclusions were obtained:

(1) The primal cause of large scatter of V_T in the surface tension force dominant regime is not the difference in surfactant concentration but the difference in initial shape deformation.
(2) Bubble motion, shape and velocity are remarkably sensitive to initial shape deformation.
(3) Small initial shape deformation results in a low V_T and a high aspect ratio, whereas large initial deformation results in a high V_T and a low aspect ratio, i.e. more deformed shape.
(4) Bubble motion is apt to be zigzag when initial shape deformation is small, whereas the transition from zigzag to helical motion is enhanced when initial shape deformation is large, as

indicated by Ellingsen and Risso.
(5) V_T possesses a strong correlation with a mean aspect ratio E.
(6) The primal role of surfactants in this regime is to cause the damping of bubble shape oscillation, by which a contaminated bubble behaves as if it were a clean bubble with low initial shape deformation.
(7) The proposed model, Eq. (48), agrees well with measured V_T.
(8) The trend of fluctuation of rising velocity is well reproduced by the proposed model.

Acknowledgements

The authors gratefully acknowledge the financial support by Japan Society for the Promotion of Science (Grant-in-Aid for Exploratory Research, No. 13875038).

Appendix A

According to Clift et al. (1978), when the bubble Reynolds number Re is high, the potential flow theory is valid not only in the vicinity of the bubble nose but also up to a certain high angle of ϕ, e.g. $\phi \simeq 160°$. Hence there is a possibility that Eq. (16) can give good prediction of V_T by specifying an appropriate angle ϕ_A for each problem of concern. It would be therefore of use to write down a V_T model which includes $m_A = \cos\phi_A$ explicitly. The derivation is simple. Substituting Eqs. (22) and (36) into Eq. (16) yields

$$\frac{1}{2}\rho_L V_T^2 \frac{(1-E_f^2)(1-m_A^2)}{f(m_A,E_f)^2 F(E_f)^2} = \frac{2\sigma E_f^{4/3}}{d\gamma^{1/3}}\left[\frac{1}{f(m_A,E_f)}+\frac{1}{f(m_A,E_f)^3}-2\right]+\frac{1}{2}\Delta\rho g d\gamma^{1/3}E_f^{2/3}(1-m_A)$$

Solving the above equation for V_T gives

$$V_T = \frac{f(m_A,E_f)}{\sqrt{(1-E_f^2)(1-m_A^2)}}F(E_f)\sqrt{\frac{4\sigma}{\rho_L d}\frac{E_f^{4/3}}{\gamma^{1/3}}\left[\frac{1}{f(m_A,E_f)}+\frac{1}{f(m_A,E_f)^3}-2\right]+\frac{\Delta\rho g d}{\rho_L}\gamma^{1/3}E_f^{2/3}(1-m_A)} \tag{A.1}$$

The proposed model, Eq. (37), was deduced by taking the limit, $m_A \to 1$, for the above equation. If we assume a spheroidal bubble shape, then $\gamma = 1$ and $E_f = E$, so that Eq. (A.1) simplifies to

$$V_T = \frac{f(m_A,E)}{\sqrt{(1-E^2)(1-m_A^2)}}F(E)\sqrt{\frac{4\sigma}{\rho_L d}E^{4/3}\left[\frac{1}{f(m_A,E)}+\frac{1}{f(m_A,E)^3}-2\right]+\frac{\Delta\rho g d}{\rho_L}E^{2/3}(1-m_A)} \tag{A.2}$$

To examine whether or not Eqs. (A.1) and (A.2) can give good predictions for V_T, we applied Eq. (A.2) to the present experimental data by setting $\phi_A = \pi/2$, i.e. $m_A = 0$. As a result, we obtained good comparisons as shown in Fig. 14. This agreement implies that (i) the potential flow theory

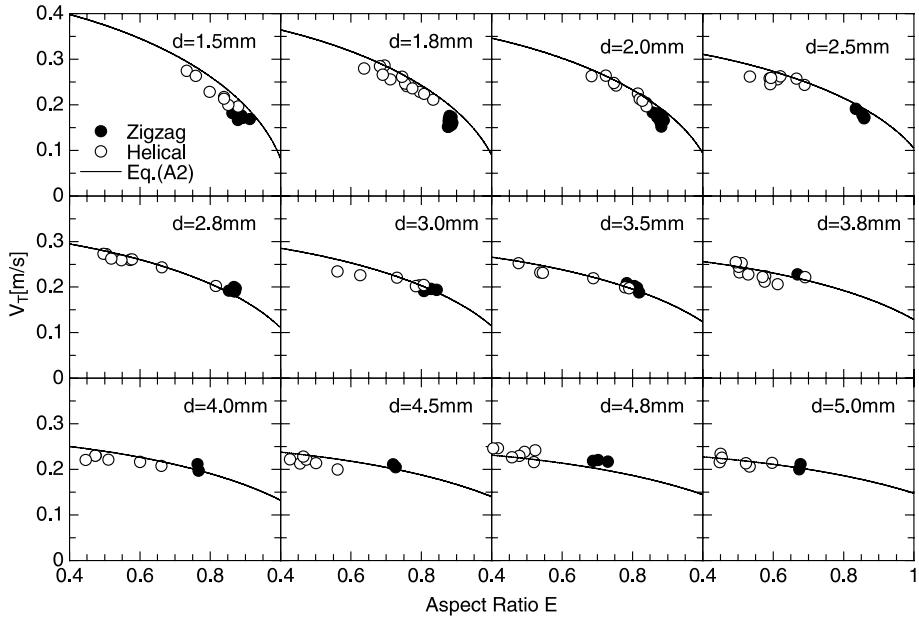

Fig. 14. Verification of Eq. (A.2) against the measured V_T for single bubbles in distilled water; $\phi_A = \pi/2$ was assumed in the calculation.

holds up to a certain high angle and (ii) Eqs. (A.1) and (A.2) are also of use in correlating experimental data.

References

Aybers, N.M., Tapucu, A., 1969. Studies on the drag and shape of gas bubbles rising through a stagnant liquid. Wärme-Stoffübertrag 2, 171–177.

Batchelor, G.K., 1967. An Introduction to Fluid Dynamics. Cambridge University Press, Cambridge, pp. 235–238.

Clift, R., Grace, J.R., Weber, M.E., 1978. Bubbles, Drops, and Particles. Academic Press, New York.

Davies, R.M., Taylor, G.I., 1950. The mechanics of large bubbles rising through extended liquid in tubes. Proc. R. Soc. Ser. A 200, 375–390.

de Vries, A., Biesheuvel, A., van Wijngaarden, L., 2001. Notes on the path and wake of a gas bubble rising in pure water. In: CD-ROM of 4th ICMF-2001, New Orleans.

Ellingsen, K., Risso, F., 2001. On the rise of an ellipsoidal bubble in water: oscillatory paths and liquid-induced velocity. J. Fluid Mech. 440, 235–268.

Ishii, M., 1975. Thermo-fluid dynamic theory of two-phase flow. Eyrolles.

Lamb, H., 1932. Hydrodynamics, sixth ed. Cambridge University Press, Cambridge.

Landau, L.D., Lifshitz, E.M., 1987. Fluid Mechanics, second ed. Pergamon Press, Oxford.

Lunde, K., Perkins, R., 1997. Observations on wakes behind spheroidal bubbles and particles. In: Proc. ASME Fluids Eng. Div. Summer Meeting, Vancouver, Canada, paper no. 97-3530.

Lunde, K., Perkins, R., 1998. Shape oscillations of rising bubbles. Appl. Sci. Res. 58, 387–408.

Magnaudet, J., Eames, I., 2000. The motion of high-Reynolds-number bubbles in inhomogeneous flows. Ann. Rev. Fluid Mech. 32, 659–708.

Marrucci, G., Apuzzo, G., Astarita, G.A., 1970. Motion of liquid drops in non-Newtonian systems. AIChE J. 16 (4), 538–541.

Mendelson, H.D., 1967. The prediction of bubble terminal velocities from wave theory. AIChE J. 13 (2), 250–253.
Peebles, F.N., Garber, H.J., 1953. Studies on the motion of gas bubbles in liquids. Chem. Eng. Prog. 49 (2), 88–97.
Saffman, P.G., 1956. On the rise of small air bubbles in water. J. Fluid Mech. 1, 249–275.
Tomiyama, A., Kataoka, I., Zun, I., Sakaguchi, T., 1998. Drag coefficients of single bubbles under normal and micro gravity conditions. JSME Int. J. Ser. B. 41 (2), 472–479.
Wellek, R.M., Agrawal, A.K., Skelland, A.H.P., 1966. Shape of liquid drops moving in liquid media. AIChE J. 12, 854–862.
Zhang, Y., Finch, J., 2001. A note on single bubble motion in surfactant solutions. J. Fluid Mech. 429, 63–66.
Zuber, N., Findlay, J.A., 1965. Average volumetric concentration in two-phase flow systems. J. Heat Transf. 87, 453–468.
Zun, I., Groselj, J., 1996. The structure of bubble non-equilibrium movement in free-rise and agitated-rise conditions. Nucl. Eng. Des. 163, 99–115.